ADVANCED MATERIALS
www.advmat.de

Ba/Ti MOF: A Versatile Heterogeneous Photoredox Catalyst for Visible-Light Metallaphotocatalysis

Krishnamoorthy Muralirajan, Il Son Khan, Luis Garzon-Tovar, Rajesh Kancherla, Nikita Kolobov, Alla Dikhtiarenko, Maram Almalki, Aleksander Shkurenko, Alejandra Rendón-Patiño, Vincent Guillerm, Khoa N. Le, Genrikh Shterk, Huabin Zhang, Christopher H. Hendon, Mohamed Eddaoudi, Jorge Gascon, and Magnus Rueping**

The field of sustainable heterogeneous catalysis is evolving rapidly, with a strong emphasis on developing catalysts that enhance efficiency. Among various heterogeneous photocatalysts, metal-organic frameworks (MOFs) have gained significant attention for their exceptional performance in photocatalytic reactions. In this context, contrary to the conventional homogeneous iridium or ruthenium-based photocatalysts, which face significant challenges in terms of availability, cost, scalability, and recyclability, a new Ba/Ti MOF (ACM-4) is developed as a heterogeneous catalyst that can mimic/outperform the conventional photocatalysts, offering a more sustainable solution for efficient chemical processes. Its redox potential and triplet energy are comparable to or higher than the conventional catalysts, organic dyes, and metal semiconductors, enabling its use in both electron transfer and energy transfer applications. It facilitates a broad range of coupling reactions involving pharmaceuticals, agrochemicals, and natural products, and is compatible with various transition metals such as nickel, copper, cobalt, and palladium as co-catalysts. The effectiveness of the ACM-4 as a photocatalyst is supported by comprehensive material studies, photophysical, and recycling experiments. These significant findings underscore the potential of ACM-4 as a highly versatile and cost-effective photoredox catalyst, providing a sustainable, one-material solution for efficient chemical processes.

1. Introduction

Developing new catalysts that utilize sustainable resources for selective cross-couplings is a compelling area of research in materials science, drug discovery, and fine chemical synthesis. Recent developments based on visible light-mediated photo-redox dual catalysis have underscored the impact of this sustainable approach in modern synthetic chemistry.[1] However, employing photocatalysts in advanced drug research often relies on precious transition-metal polypyridyl complexes or organic dyes, which often present practical limitations in terms of availability, cost, and the intricate adjustment of redox potentials, as well as challenges related to scalability and recyclability. Conversely, heterogeneous photoredox catalysis presents a promising alternative, distinguished by its environmentally friendly, scalable, and cost-effective nature, and its ability to facilitate distinctive transformations under visible light irradiation.[2] To date, two main approaches have been explored

K. Muralirajan, R. Kancherla, H. Zhang, M. Rueping
KAUST Catalysis Center (KCC)
King Abdullah University of Science and Technology
Thuwal 23955-6900, Saudi Arabia
E-mail: magnus.rueping@kaust.edu.sa

I. S. Khan, L. Garzon-Tovar, N. Kolobov, A. Rendón-Patiño, G. Shterk, J. Gascon
KAUST Catalysis Center (KCC)
Advanced Catalytic Materials (ACM)
King Abdullah University of Science and Technology
Thuwal 23955-6900, Saudi Arabia
E-mail: jorge.gascon@kaust.edu.sa

The ORCID identification number(s) for the author(s) of this article can be found under https://doi.org/10.1002/adma.202405646

DOI: 10.1002/adma.202405646

A. Dikhtiarenko
Imaging and Characterization Department
KAUST Core Labs
King Abdullah University of Science and Technology (KAUST)
Thuwal 23955, Saudi Arabia

M. Almalki, A. Shkurenko, V. Guillerm, M. Eddaoudi
Functional Materials Design, Discovery and Development Research Group (FMD3)
Division of Physical Sciences and Engineering
King Abdullah University of Science and Technology (KAUST)
Thuwal 23955-6900, Saudi Arabia

K. N. Le, C. H. Hendon
Department of Chemistry and Biochemistry
University of Oregon
Eugene, OR 97403, USA

in the design of heterogeneous photocatalysts: i) employing organic and inorganic semiconductors as photocatalysts,[3] and ii) embedding active photosensitizers (metallic/non-metallic) into porous materials (vide infra).[4] The first approach may encounter challenges such as inadequate light absorption, the presence of harmful/ undesirable components, limited tunability, and morphology and surface-sensitive nature that diminish efficiency. In contrast, the second approach improves the controlled dispersion of active photoactive species, exemplified by the integration of well-defined polypyridyl metal complexes into MOFs.

MOFs have received attention as photocatalysts owing to their intrinsic characteristics, including high porosity, structural stability, and reusability.[5] With the careful selection of building blocks (metal ions and ligands), materials with specific light-harvesting properties can be tailored for targeted applications.[5a] However, despite the precise control over the structure of MOFs, many tested as photocatalysts exhibit limited reactivity in organic synthetic applications. Overcoming these limitations, the successful incorporation of photoactive complexes (Ru, Ir, and EY) into MOFs was achieved and utilized in single-electron transfer (SET) reactions.[4] In 2018, Lin and co-workers successfully developed a stable Zr_{12}-MOFs (Zr_{12}-Ir-Ni) catalyst by elegantly integrating Ir(III) photoredox and Ni(II) cross-coupling catalysts.[4a] Subsequently, the same group reported a Hf_{12}-Ir-Ni MOF prepared by integrating Hf_{12} secondary building units (SBUs) with both Ir(DBB)[dF(CF_3)ppy]$^+$ photocatalytic bridging ligands and Ni(MBA)Cl_2 complexes.[4d] More recently, an interesting dual metalation strategy in a single 2D Covalent Organic Framework (COFs), Ni−Ir@TpBpy COFs, was demonstrated.[4b] Although the design of these systems is elegant and has facilitated photoredox cross-couplings, the use of Ir as the light-absorbing species remains essential. Reports of heterogeneous photoactive materials capable of participating in a variety of reactions, employing both single electron transfer (SET) and energy transfer in conjunction with different metal catalysts for the synthesis of complex molecules, have yet to be realized.

Ti-based MOFs hold promise as photocatalysts due to their high chemical stability and the presence of low-lying, vacant 3d orbitals in Ti^{4+}, which are crucial for the ligand-to-metal charge transfer (LMCT) process.[6] However, synthesizing new Ti-based MOFs remains challenging due to the complex chemistry of titanium in solution.[7] In this report, we present a novel, multifunctional heterometallic Ba/Ti-based MOF, that acts as a versatile heterogeneous visible light photocatalyst for a range of C–X (X = C, O, S, N) cross-coupling reactions through energy transfer (EnT) and electron transfer (ET) processes. The design of this MOF photocatalyst was guided by several criteria: i) the creation of heterometallic secondary building units (SBUs) that mimic the composition of the inorganic semiconductor $BaTiO_3$, and ii) the incorporation of a photoactive, electron-rich pyrene-based ligand that facilitates the formation of high-lying, flat bands due to the delocalized π-electrons in the pyrene unit.[8] This combination of highly mobile electrons and strong hole localization at pyrene-based ligands has been shown to enhance hydrogen production during the photocatalytic hydrogen evolution reaction (HER).[9]

2. Results and Discussion

To construct the new heterometallic MOF (**ACM-4**) according to the specified criteria, a solvothermal reaction was carried out using $BaCl_2$, bis(cyclopentadienyl) titanium(IV) dichloride, and 4,4′,4′′,4′′′-(pyrene-1,3,6,8-tetrayl)tetrabenzoic acid (H_4TBAPy), with acetic acid as a modulator (see Supporting Information). After 48 h, yellow rod-shaped crystals were obtained (Figure S1, Supporting Information). Despite the multiple attempts to obtain single crystals suitable for single-crystal X-ray diffraction (SCXRD), the structural model of **ACM-4** was constructed based on the structure and atomic positions of the isostructural monometallic Ba-based MOF, which was successfully crystallized and characterized (Table S1, Supporting Information). Le Bail profile refinement confirmed that **ACM-4** is indeed isostructural to the monometallic Ba-MOF, revealing that **ACM-4** crystallizes in the monoclinic *C2/c* space group with unit cell parameters of a = 25.424(16) Å, b = 21.670(6) Å, and c = 7.535(7) Å (Figure S2, Supporting Information). The structural model that includes Ba/Ti atoms occupying the same crystallographic position was subjected to Rietveld refinement, which revealed that the atomic occupancies of barium and titanium atoms at the same position have an occupation disorder with occupancy factors of 0.598(9) and 0.402(9), respectively (Figure S3; Table S2, Supporting Information). This means that **ACM-4** contains five barium and three titanium atoms per unit cell and can be described by the empirical formula accounting for counterbalanced chlorine anions as $[Ba_{0.6}Ti_{0.4}O_5H_{11}C_{22}]Cl_{0.8}$. In **ACM-4**, the infinite inorganic molecular building blocks consist of Ba/TiO_3 rods constructed from 8-coordinated metal centers. Each Ba/Ti is coordinated to eight oxygen atoms from carboxylates of six linkers, resulting in infinite rods of edge-shared Ba/TiO_8 polyhedra along the *c* direction. These rods are extended in six directions by TBAPy linkers, which connect each rod to eight neighboring rods in the *a* and *b* directions. This structure generates 1D rectangular channels with a height of ≈3.5 Å and width of ≈7.0 Å (dimensions considering van der Waals radii, **Figure 1a**). Topological analysis based on the general method for road-building unit-based MOFs revealed that the topology of **ACM-4** corresponds to an unprecedented (4,5)-c net with transitivity [2 2] (Figure S4, Supporting Information).

Scanning Electron Microscopy (SEM) further confirmed the homogeneous formation of rod-shaped crystals, and the Energy Dispersive X-ray Spectrometry (EDX) elemental mapping revealed a highly uniform distribution of Ti and Ba atoms along the crystals (Figure 1b; Figures S5 and S6, Supporting Information). This agrees with the X-ray photoelectron spectroscopy (XPS) analysis, which confirmed the presence and expected oxidation states of the elements present in the SBU of **ACM-4**. As shown in Figure S7a (Supporting Information), two bands at binding energies of 458.9 and 464.7 eV are attributed to Ti $2p_{3/2}$ and $2p_{1/2}$, respectively, corresponding to the Ti^{4+} oxidation state.[10] Additionally, the binding energy of the Ba 3d band at 780.2 eV corresponds to Ba^{2+} species (Figure S7b, Supporting Information).[11] The content of Ba and Ti in **ACM-4** was estimated by inductively coupled plasma-optical emission spectroscopy (ICP-OES), from which a Ti: Ba ratio of 1: 1.6 was determined (Table S3, Supporting Information). This result agrees with the chemical formula of

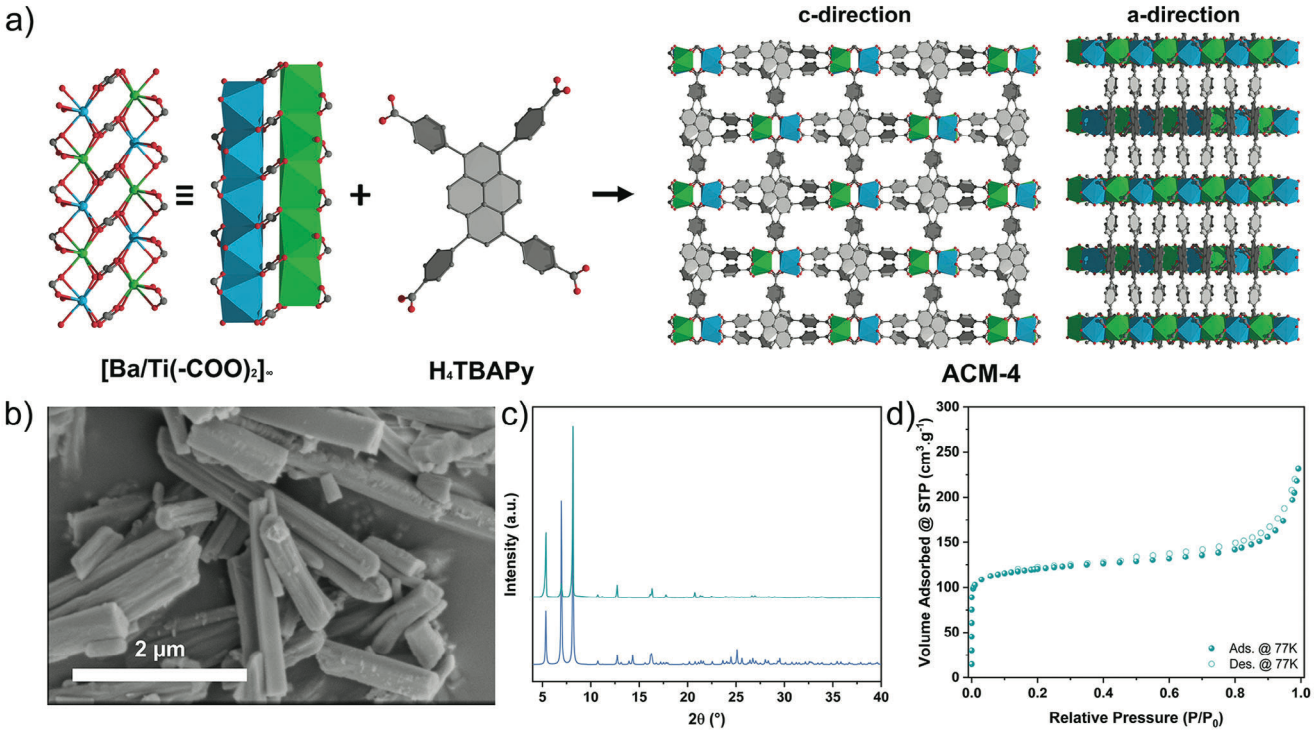

Figure 1. a) Schematic representation of the **ACM-4** framework along the *c* axis showing the assembly of the [Ba/Ti(-COO)$_2$] SBU with the 4-connected H_4TBAPy ligand. Color code: C, gray; O, red; Ba, blue; and Ti, green. b) SEM image of **ACM-4** showing the rod-shaped crystals. c) PXRD pattern of **ACM-4** (turquoise) compared with the simulated pattern and d) N_2 adsorption isotherm of **ACM-4**.

ACM-4. The phase purity of the **ACM-4** material was confirmed by powder X-ray diffraction (PXRD) (Figure 1c).

The thermal stability of **ACM-4** was evaluated by thermogravimetric analysis (TGA) and variable-temperature powder X-ray diffraction (VT-PXRD), revealing that the material retained its crystallinity up to 300 °C (Figure S8, Supporting Information). The chemical robustness of **ACM-4** was studied by immersing it in deionized water at different pH levels and in some common organic solvents for 24 h. The PXRD patterns of the solids confirmed that their crystallinity was not affected after exposure to organic solvents and aqueous solutions within a pH range of 5–9 (Figure S9, Supporting Information). Under more aggressive alkaline (pH $\geq$ 11) or acidic (pH $\leq$ 3) conditions, the PXRD patterns show noticeable peak broadening and the appearance of new peaks. The porosity of **ACM-4** was examined by nitrogen adsorption-desorption measurements, exhibiting a type I isotherm, which confirms its microporous nature (Figure 1d; S10, Supporting Information). The Brunauer-Emmett-Teller specific surface area (S_{BET}) was calculated to be 462 $m^2\ g^{-1}$. The total pore volume was estimated to be 0.20 $cm^3 g^{-1}$ at $P/P_0 = 0.5$, in agreement with the theoretical value (0.19 $cm^3 \cdot g^{-1}$). By using the non-local density functional theory (NLDFT) model, the average pore size of **ACM-4** was found to be 8.4 Å, which is consistent with the crystallographic data (Figure S10d, Supporting Information).

Subsequently, we investigated the optical properties of **ACM-4** to assess its potential as a photoredox catalyst. Pyrene-derived compounds are known for their visible-light absorption, energy-transfer ability, and long excited-state lifetime.[8,9] The light absorption properties of **ACM-4** were examined by diffuse reflectance ultraviolet–visible (UV–vis) spectroscopy. The UV–vis spectra (Figure S11, Supporting Information) exhibited a broad band ≈490 nm, which is slightly blue-shifted compared to the parent H_4TBAPy ligand (light absorption up to 500 nm). The experimental optical bandgap of **ACM-4**, determined via a Tauc plot, was found to be 2.6 eV (Figure S12, Supporting Information). By combining this value with the valence band (HOCO) value of 5.8 eV (vs vacuum level), which was determined by photoelectron spectroscopy in air (PESA) (Figure S13, Supporting Information), we were able to determine the conduction band (3.2 eV) and construct the band alignment diagram of **ACM-4** as shown in Figure S14 (Supporting Information).

Considering the presence of Ti in the MOF structure, the ligand-to-metal charge transfer (LMCT) mechanism was confirmed by solid-state electron paramagnetic (EPR) spectroscopy. Under illumination in the presence of triethylamine as a sacrificial agent, the characteristic Ti^{3+} signals with $g_\perp = 1.966$ and $g_\parallel = 1.934$ were observed (Figure S15, Supporting Information). It is important to point out that MOFs featuring LMCTs (i.e., MIL-125-NH_2) are desirable for photocatalytic applications[6,12] due to their efficient charge separation and longer charge carriers lifetime.[9,13] Indeed, electronic band structure (EBS) and density of states (DOS) calculations using density functional theory (DFT) revealed that both the conduction band and the valence band are relatively flat (Figure S18a, Supporting Information). The valence band is dominated by the π-orbitals of the TBAPy linker, while the conduction band exhibits contributions from both the TBAPy linker and the Ti-3d orbitals, indicating a hybrid

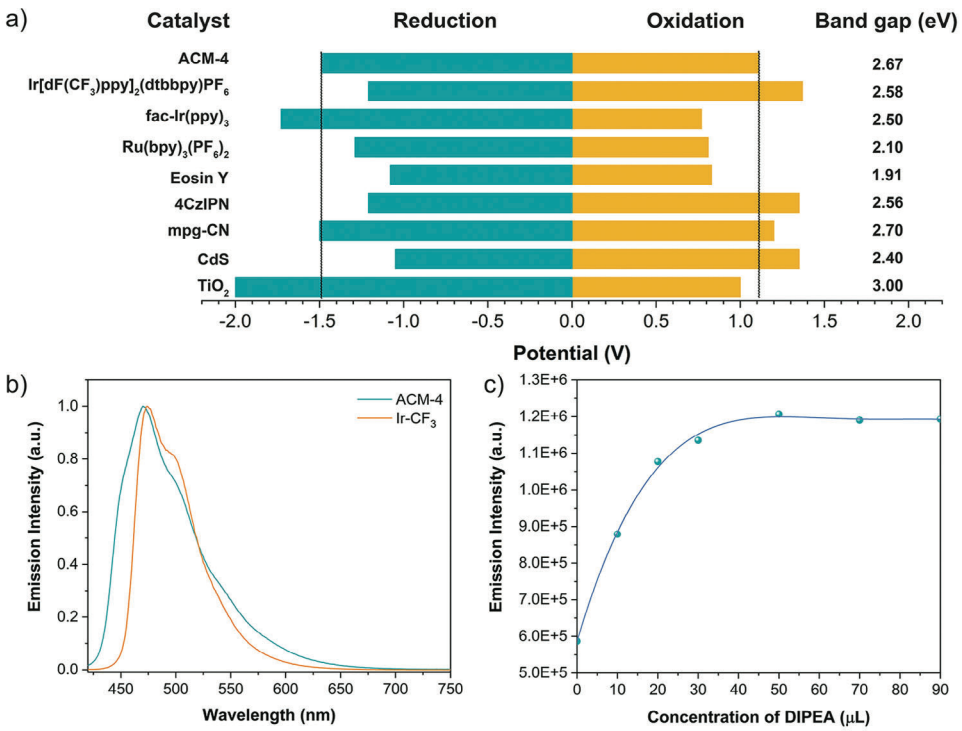

Figure 2. Comparison of commonly used photocatalysts versus **ACM-4**. a) Reduction, oxidation potentials, and bandgap of common photocatalysts with **ACM-4**. b) Emission spectra of **ACM-4** and $Ir[dF(CF)_3ppy]_2(dtbbpy)PF_6$. c) Reverse emission quenching of [ACM-4 + $NiBr_2 \cdot 3H_2O$] with *N*,*N*-diisopropylethylamine (DIPEA).

character (Figure S18, Supporting Information). This hybridization results in a conduction band with reduced dispersion compared to systems dominated purely by Ti orbitals.[9,14] This suggests that excitation might primarily occur within the linker, with partial charge transfer to the Ti centers due to the close energy levels of the Ti-3d orbitals, as further supported by EPR data affirming the presence of Ti^{3+} species. This confirms that the photocatalytic process of **ACM-4** involves a ligand-to-metal charge transfer mechanism. In addition, Ti centers are likely to play a more significant role than Ba centers due to the lack of Ba-DOS in the conduction band or valence band. Nevertheless, it has been demonstrated that the presence of Ba^{2+} might lead to the stabilization of Ti orbitals, reducing the conduction band level by ≈100 meV.[11] Finally, the electronic band structure also revealed that **ACM-4** has a direct bandgap of 2.28 eV, closely aligning with the experimental measurement, and the computational ionization potentials were found to be in excellent agreement with those obtained experimentally.

The broad redox potential range, spanning from +1.11 to −1.49 V versus saturated calomel electrode (SCE), allows for both the reduction and oxidation of transition metals as well as a wide variety of organic substrates. Notably, the 2.6 eV bandgap is comparable to or slightly larger than those of frequently used Ir-photoredox complexes, organic dyes, and metal semiconductors (**Figure 2A**).[3e,15] Most importantly, the triplet energy of **ACM-4** (ΔE = 60.8 kcal mol^{-1}) is almost similar or higher than the commonly used conventional photosensitizers ($Ir[dF(CF)_3ppy]_2(dtbbpy)PF_6$, ΔE = 60.7 kcal mol^{-1}; $Ir(ppy)_3$, ΔE = 53.6 kcal mol^{-1}) (Figure 2B; Figure S19, Supporting Information), which warrant its use as an energy transfer photocatalyst.

2.1. ACM-4/Ni Photoredox Dual Catalysis

Recently, it was shown that the challenging reductive elimination steps from either electronically excited Ni(II) or Ni(III) intermediates can be eased through energy transfer (EnT) or electron transfer (ET) from an iridium photosensitizer.[16] Given the adequate redox potentials, bandgap, and high triplet energy of **ACM-4**, we anticipated that the photosensitization of Ni complexes by **ACM-4** could result in efficient organic transformations. Recently, nickel has emerged as a prominent catalyst for facilitating various carbon-heteroatom cross-coupling reactions in its excited state. However, the need for short excitation wavelengths in the purple region, elevated reaction temperatures, and the reliance on more reactive aryl halides pose limitations that impact the generality and the economic viability of the reactions.[17] Developing sustainable photocatalysts for the effective transformation of organic molecules into high-value-added compounds is a key objective in cutting-edge academic and industrial research and development.[18] In modern drug design and discovery, the modification of heterocycles and natural products, as well as their combination via cross-couplings, is essential.[19] Many drugs feature aryl or aliphatic substituents with polar functionalities involving nitrogen, oxygen, and sulfur compounds-which are crucial for maximizing drug-target interactions and maintaining optimal pharmacokinetics.[20] However, these polar functional groups can

present challenges in cross-coupling reactions due to the Lewis basic nature of substrates or the high reactivity of cross-coupling transition-metal catalysts, leading to catalyst poising and substrate decomposition. Thus, there is a need for improved methods that are milder and compatible with a broad range of functional groups.[21]

We initiated our investigation with a carbon-oxygen (C–O) cross-coupling reaction, using **ACM-4** in combination with a Ni-complex and irradiating at 440 nm at room temperature conditions. Optimization studies revealed that the treatment of benzoic acid with methyl 4-bromobenzoate in the presence of $NiCl_2$-dtbbpy co-catalyst, *N*-tert-butylisopropylamine (BIPA) base, and DMA solvent yielded the desired C–O cross-coupled product **1** in 92% yield (Table S4, Supporting Information). Further improvement in yield to 97% was observed using Cs_2CO_3 as the base under the standard conditions. Comparative reactions with the H_4TBAPy linker, and other MOFs such as MIL-125-(NH_2) and the monometallic Ba-MOF, established **ACM-4** as an effective catalyst for the C–O cross-coupling reaction (Table S5, Supporting Information). Further, control experiments in the absence of **ACM-4**, nickel, ligand, or a base did not result in the cross-coupling product **1**, underscoring the pivotal role of **ACM-4** and other individual components in the catalysis. While higher wavelengths of light (480 and 540 nm) also yielded the C–O cross-coupled product **1** in 58% and 31% yield, respectively, the 440 nm wavelength was found to be more effective (Table S5, Supporting Information).

To better understand the superior activity of **ACM-4** compared to MIL-125-(NH_2), we performed electrochemical measurements to assess the charge transfer efficiency and the generation of photoinduced charges. Specifically, we conducted photocurrent measurements and Electrochemical Impedance Spectroscopy (EIS) for both **ACM-4** and MIL-125-(NH_2).[22] The transient photocurrent was measured under on-off cycles using visible light (λ > 420 nm) in a 0.5 M Na_2SO_4 aqueous solution. As illustrated in Figure S16 (Supporting Information), **ACM-4** exhibited a higher photocurrent response, consistent with its superior photocatalytic performance. Additionally, EIS analysis at high frequencies indicated faster interfacial charge transfer for MIL-125-(NH_2) compared to **ACM-4**. However, in the low-frequency range, MIL-125-(NH_2) displayed a vertical curve indicative of non-ideal capacitance. While increased capacitive behavior can potentially enhance photocatalytic activity by capturing and storing more photogenerated electrons, excessive charge accumulation can lead to recombination,[23] which may explain the lower photocurrent observed for MIL-125-(NH_2).

Based on literature reports[24] and our previous findings,[25] we propose a mechanistic pathway for the C–O cross-coupling involving an energy transfer from **ACM-4** (ΔE = 60.8 kcal mol^{-1}) to Ni(II) intermediate (Scheme S1, Supporting Information).[26] The steady-state Stern-Volmer quenching studies using different concentrations of $NiBr_2{\cdot}3H_2O$ (**Ni-1**) as quencher revealed significant quenching of **ACM-4**, indicating that Ni(II) can be initially reduced by **ACM-4** under visible light (Figures S20–S22, Supporting Information). The reduced low valent-Ni then undergoes oxidative addition with aryl bromide to form a Ni(II)-aryl bromide intermediate (**Ni-2**), which further undergoes nucleophilic exchange with benzoate to give aryl-Ni(II)-benzoate complex (**Ni-3**). **Ni-3** can then undergo reductive elimination via energy transfer from **ACM-4** to yield the C–O cross-coupling product. To confirm the energy transfer from **ACM-4** to **Ni-3**, we conducted quenching studies using variable concentrations of **Ni-3** (prepared in situ, Figure S26, Supporting Information), which showed significant quenching of **ACM-4**, asserting the energy transfer process (Figures S27–S29, Supporting Information). Additionally, a catalytic reaction using **Ni-3** and **ACM-4** in DMA under visible light irradiation produced the expected C–O cross-coupled product **2**, supporting the energy transfer mechanism (Scheme S1, Supporting Information). It is important to mention that our further carbon–hetero atom (C–OR, C–OH, C–SR, C–NR) cross-coupling examinations with **ACM-4** and Ni-catalyst delivered a similar catalytic transformation at room temperature (Tables S7–S25, Supporting Information). Nevertheless, the possibility of an electron transfer (ET) mechanism in these reactions cannot be completely ruled out (Scheme S2, Supporting Information).[24b] For instance, in the case of aniline synthesis (Tables S24 and S25, Supporting Information), the $NiBr_2.3H_2O$ (**Ni-1**) can initially be reduced by **ACM-4**, and the resulting reduced Ni(I) undergoes oxidative addition with aryl bromide to form an aryl-Ni(III)-bromide intermediate. This Ni(III) intermediate can then undergo nucleophilic exchange with sodium azide (NaN_3) to produce the C–N cross-coupled product **90** (Scheme S2). To verify our hypothesis, we performed the quenching experiments using different concentrations of *N,N*-diisopropylethylamine (DIPEA) as the quencher, which does not quench the **ACM-4**, indicating that excited-state **ACM-4** is not initially reduced by the amine (Figures S34 and S35, Supporting Information). This suggests that **ACM-4** can only be oxidized in its excited state through the reduction of $NiBr_2{\cdot}3H_2O$ (**Ni-1**) (Figures S20–S22, Supporting Information). To verify the presence of oxidized **ACM-4** during the reaction, reverse quenching experiments were performed using a mixture of **ACM-4** and a high concentration of **Ni-1** as the standard, with DIPEA serving as the quencher. We anticipated that the mixture of **ACM-4** and a high concentration of **Ni-1** would produce oxidized **ACM-4** (Figure S36, Supporting Information), which could then be quenched by the DIPEA if our hypothesis was correct. As expected, increasing the concentration of DIPEA resulted in the regeneration of **ACM-4**, as confirmed by direct visualization and reverse emission quenching experiments (Figure 2C; Figures S37–S39, Supporting Information), demonstrating the electron transfer from DIPEA to the oxidized **ACM-4**. To exclude the possibility of an energy transfer mechanism in aniline synthesis, an aryl-Ni(II)-azide complex (prepared in situ) from a stable aryl-Ni(II)-Br (**Ni-2**) complex was tested under standard reaction conditions, which did not yield the expected C–N cross-coupled product **90**, supporting that the reductive elimination is taking place from the Ni(III) intermediate via an electron transfer mechanism. Overall, **ACM-4** enables efficient energy and electron transfer with nickel, which is attributed to its ligand-to-metal charge transfer properties, combined with its large bandgap, broad redox potential range, and high stability, facilitating a variety of cross-coupling reactions (Tables S4–S25, Supporting Information).

Building on the optimization studies with **ACM-4** and Ni, we explored the scope of carbon-heteroatom cross-coupling reactions using a variety of nucleophiles and aryl halides, with a particular focus on pharmaceuticals, agrochemicals, and natural products (**Figures 3–5**). We initially focused on coupling aryl bromides with bioactive molecules, such as natural products

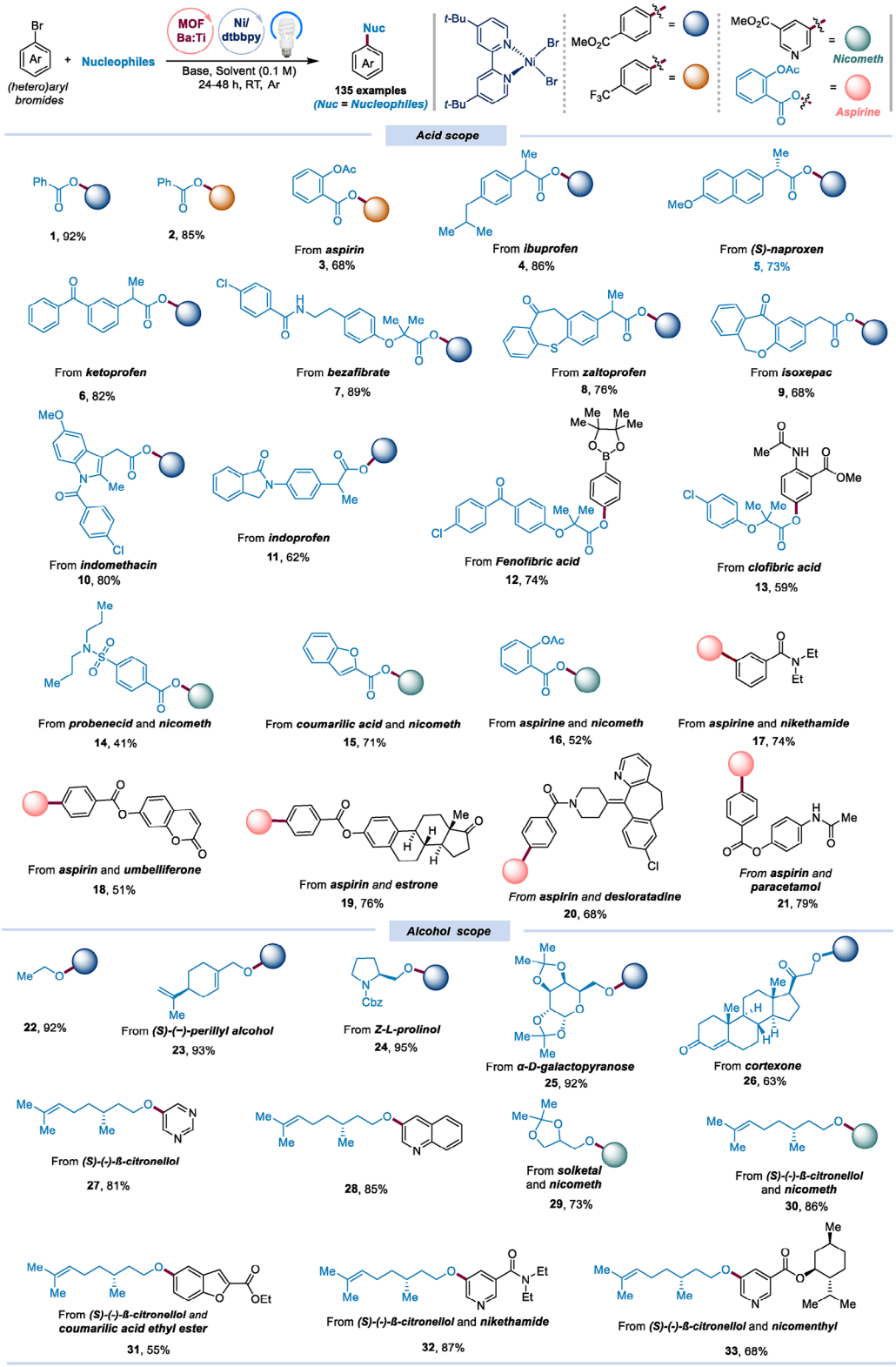

Figure 3. Substrate scope using bioactive acids and alcohols as the nucleophiles in the **ACM-4**/nickel-catalyzed cross-couplings. See the Supporting Information for detailed reaction conditions for each substrate; yields are isolated.

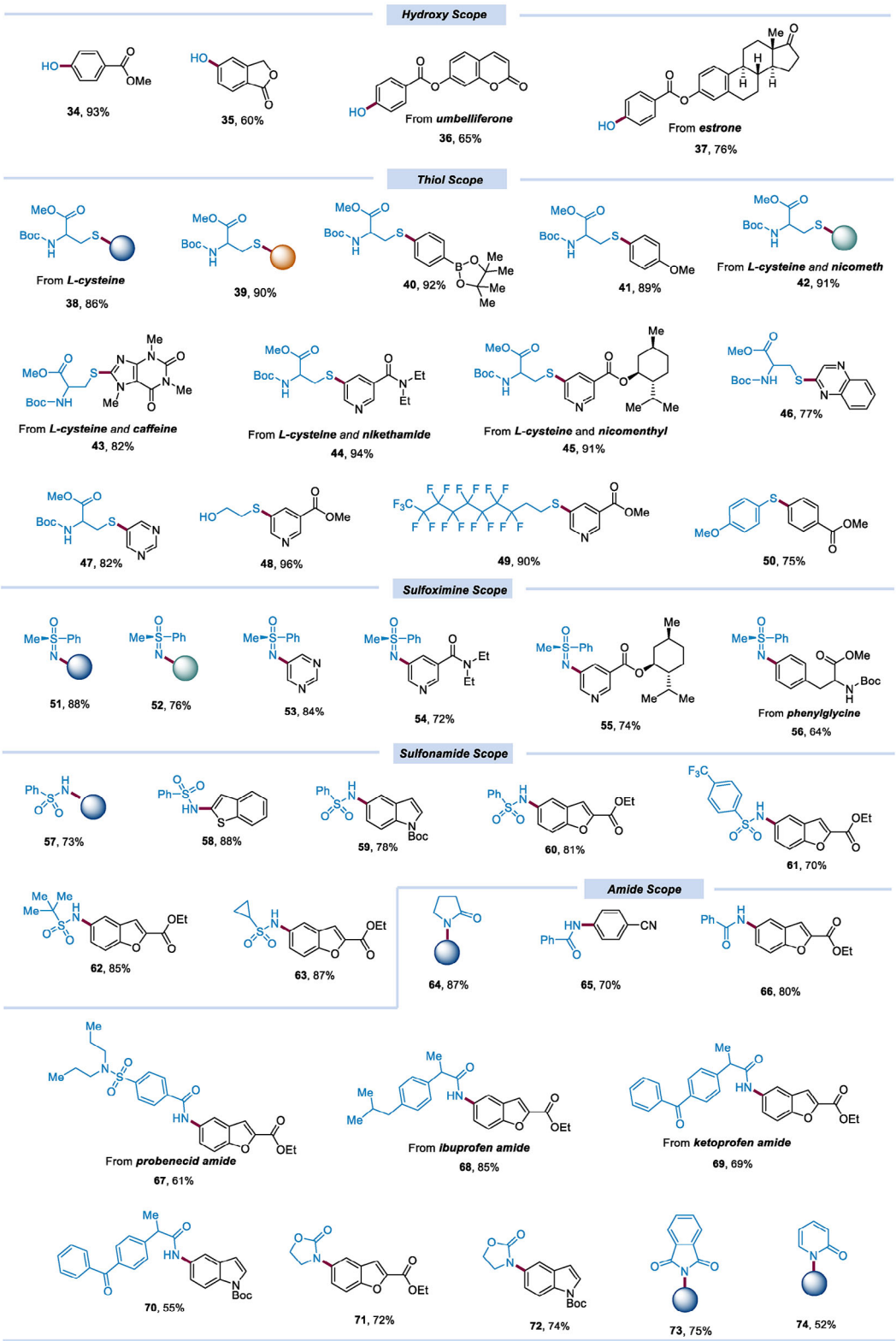

Figure 4. Substrate scope using water, thiols, sulfoximines, sulfonamides, and amides as the nucleophiles in the **ACM-4**/nickel-catalyzed cross-couplings. See the Supporting Information for detailed reaction conditions for each substrate; yields are isolated.

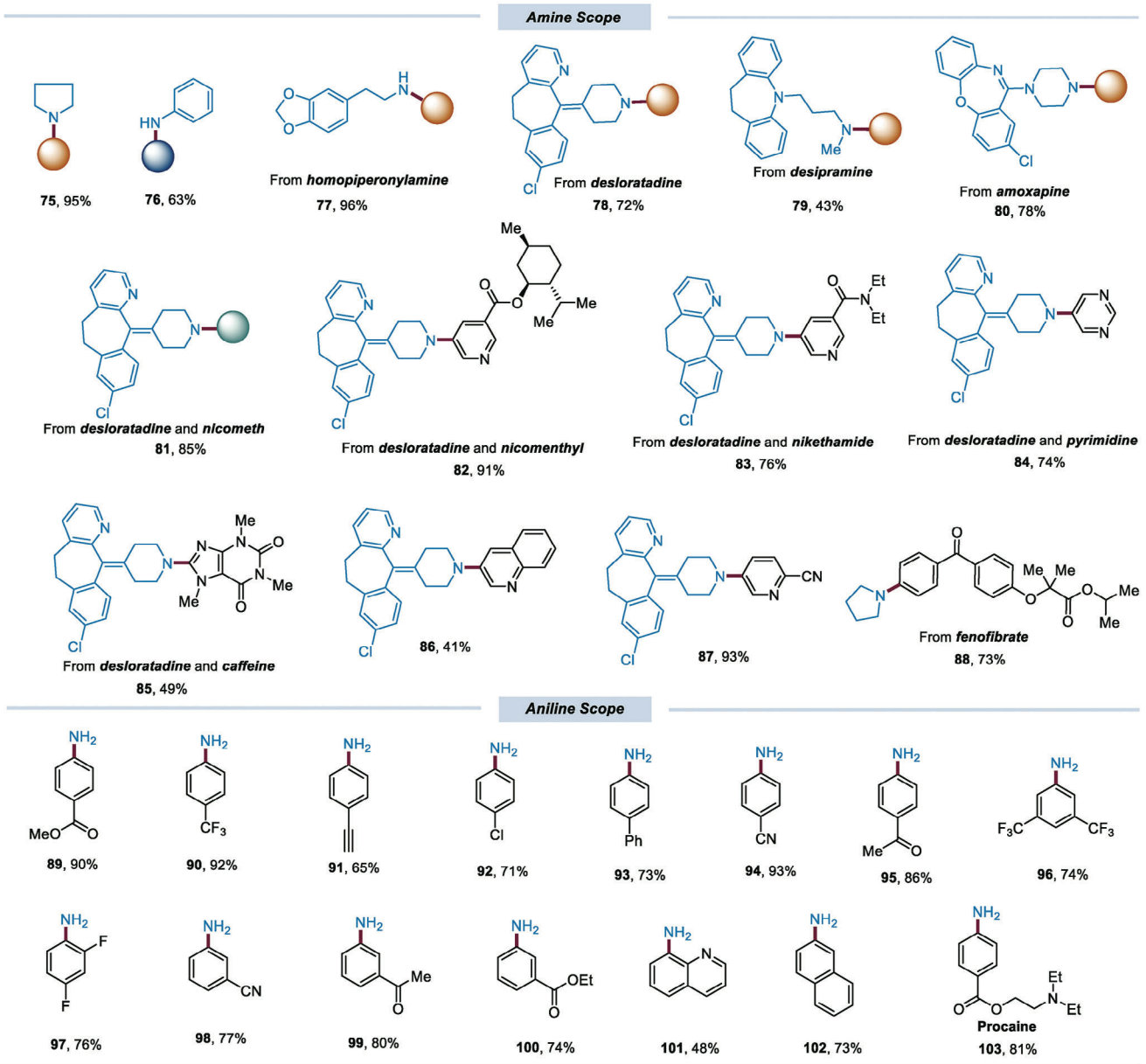

Figure 5. Substrate scope using amines and azide as the nucleophiles in the **ACM-4**/nickel-catalyzed cross-couplings. See the Supporting Information for detailed reaction conditions for each substrate; yields are isolated.

and pharmaceuticals with acid functionality (Figure 3), which resulted in excellent reactivity, yielding aryl esters **3–21** (up to 89%). The scope of the reaction is remarkable, as a variety of acid nucleophiles with different functional groups-capable of coordinating to the Ti centers in **ACM-4**-were well tolerated, with no adverse effect on the stability of the MOF. Drug derivatives containing acid groups, including aspirin (**3**), ibuprofen (**4**), (*S*)-naproxen (**5**), ketoprofen (**6**), bezafibrate (**7**), zaltoprofen (**8**), isoxepac (**9**), indomethacin (**10**), indoprofen (**11**), fenofibric acid (**12**), clofibric acid (**13**), probenecid (**14**), and coumarillic acid (**15**), were found to be compatible. Notably, drug moieties with aryl bromides such as nicometh (used in biarylcarboxamide inhibitors for treating rheumatoid arthritis), nikethamide (analeptic agent), umbelliferone, estrone, desloratadine, and paracetamol were effectively coupled, resulting in moderate to good yields of the C–O cross-coupled product **14–21**. We then shifted our focus to investigate the versatility of this dual catalysis concerning other nucleophiles such as alcohols, hydroxyl, and thiols (Figures 3,4). We employed (*S*)-perillyl, Z-L-prolinol, α-D-galactopyranose, certexone, (*S*)-(-)-β-citronellol, solketal as oxygen nucleophiles, resulting in the formation of ether derivatives **23–29** in 63%–95% yields. Additionally, the cross-coupling of (*S*)-(-)-β-citronellol (used in perfumes and insect repellents) with bromo-substituted drug molecules such as nicometh, coumarilic acid ester, nikethamide, and nicomenthyl (employed in anti-aging, anti-free radical, anti-pollutant, skin detox, and sun care products) yielded hybrid drug molecules

30–33 in good yields (55%–87%). Remarkably, hydroxylation of aryl halides using water under ACM-4/Ni photochemical conditions produced phenolic compounds **34–37** in good yields, without catalytic decomposition (Figure 4). Additionally, the sulfur-containing amino acid L-cysteine was used as a nucleophile in the presence of **ACM-4**/Ni, leading to the formation of L-cysteine-substituted thioethers **38–47** with excellent yields (up to 94%). Furthermore, this approach was successfully applied to a range of aliphatic and aromatic thiols, resulting in high conversion up to 96% (**48–50**).

The efficiency of the **ACM-4**/Ni dual catalysis was further demonstrated by successfully conducting the reaction involving nitrogen-containing coupling partners such as sulfoximines, sulfonamides, and amide derivatives with weak nucleophilicity (Figure 4). Various aryl and alkyl *N*-nucleophiles were tested in C–N cross-coupling reactions with different aryl bromide drug analogues, delivering the target bulky molecules **51–74** in good yields. Notably, the use (*S*)-(+)-*S*-methyl-*S*-phenylsulfoximine (**51—56**), probenecid amide (**67**), ibuprofen amide (**68**), ketoprofen amide (**69**), 2-oxazolidone (**71** and **72**), and 2-pyridone (**74**) as coupling partners to access pharmaceutical derivatives were realized for the first-time using MOF/Ni cooperative catalysis at room temperature. To further demonstrate the versatility of our dual catalysis approach, direct C–N cross-coupling was carried out by reacting amine-containing drug compounds with aryl bromides under standard conditions (Figure 5). For instance, homopiperonylamine, desloratadine, desipramine, and amoxapine were reacted with 4-bromobenzotrifluoride in the absence of ligand, yielding the expected C–N cross-coupled products **75–88** in good yields. Finally, the synthesis of free anilines via reductive aromatic amination with sodium azide as the amine source also proceeded smoothly using our dual catalytic system at room temperature.

This protocol was compatible with a range of functional group-substituted aryl bromides, resulting in free aniline products **89–103** in good to excellent yields (48%–93%). Notably, this method also facilitated the direct synthesis of drugs such as procaine (**103**) in 81% yield. Overall, the use of **ACM-4** in cooperative Ni-catalysis showcases remarkable stability and consistent reactivity across a range of catalytic processes. Its ability to efficiently catalyze reactions with diverse organic substrates, including more challenging ones, highlights its robustness and adaptability, even in the presence of various coordinating molecules. This versatility is especially beneficial for synthetic applications, particularly in industrial settings, as it demonstrates **ACM-4**'s ability to accommodate a range of functional groups and molecular frameworks.

Encouraged by these results, we further explored the photocatalytic activity of **ACM-4** in combination with other transition metals, including copper, cobalt, and palladium, across a range of cross-coupling reactions (**Figure 6**, also see the supporting information for full details).

2.2. ACM-4/Cu Photoredox Dual Catalysis

Initially, we decided to explore decarboxylative cyanation reactions using synergistic **ACM-4** photoredox and copper catalysis with *N*-hydroxy-phthalimide (NHP) esters and trimethylsilyl cyanide (TMSCN) under visible light irradiation at RT. We were pleased to find that the photochemical decarboxylative cyanation reaction was highly effective with an ibuprofen NHP ester derivative, yielding the desired cyanation product **104** in 95% (isolated 89%) yield under mild reaction conditions using NMP as solvent (Table S26, Supporting Information). Control experiments confirmed that both **ACM-4** and the copper catalyst are essential for the success of the decarboxylative cyanation (Table S27, Supporting Information). Comparative studies using the monometallic **Ba-ACM-4** MOF (28% yield) and TBAPy linker (0% yield) demonstrated that **ACM-4** is an effective catalyst for the proposed transformation. Irradiation at a wavelength of 440 nm is essential for optimal results, as higher wavelengths (480 and 540 nm) resulted in significantly lower yields (Table S27, Supporting Information). With the optimized reaction conditions in hand, other NHP esters were further examined to explore the scope of the reaction. As shown in Figure 6a, various NHP esters derived from biologically active carboxylic acids, such as naproxen, ketoprofen, isoxepac, indomethacin, fenofibric, 2,4-dichlorophenoxyacetic, and 5-oxo-5-phenylvaleric acid, were compatible with the reaction conditions, producing cyanation products **105–111** in yields up to 93%. Further, to highlight the synthetic utility of our MOF dual catalysis protocol, we extended it to multicomponent decarboxylative cyanoalkylation reactions involving alkenes (styrenes and 1,3-dienes), NHP esters, and TMSCN. A range of functional groups, including methyl, *tert*-butyl, phenyl, nitrile, trifluoromethyl, chloride, and carboxylate, were well tolerated, yielding corresponding cyanoalkylation products **112–121** in good to excellent yields. In these cyanoalkylation reactions, **ACM-4** ($E_{1/2}$ = −1.49 V vs SCE) acts as a photo-reductant, converting NHP esters into alkyl radicals (e.g., 1,3-dioxoisoindolin-2-yl 2-(4-isobutylphenyl)propanoate; $E_{1/2}$ = −1.33 V vs SCE) via a SET mechanism. Concurrently, the oxidized form of **ACM-4** ($E_{1/2}$ = +1.11 V vs SCE) is reduced by oxidizing Cu(I) ($E_{1/2}$ = +0.36 V vs SCE) to Cu(II), thereby regenerating the active **ACM-4**. The Cu(II) species then reacts with TMSCN and combines with the alkyl radical to yield the cyanoalkylation product and Cu(I) (Scheme S3, Supporting Information).

2.3. ACM-4/Co Photoredox Dual Catalysis

Building on the success of the MOF/Cu cooperative catalysis, we subsequently extended our methodology to a distinct reaction: the direct C–H functionalization of arenes by combining **ACM-4** with cobalt catalysis at room temperature (Figure 6a). Remarkably, the combination of **ACM-4** with cobalt demonstrates exceptional reactivity in the mild C–H oxidative annulation of amides with alkynes or alkenes, leading to the formation of annulated products **122–123** in good yields. Control experiments demonstrate **ACM-4** as an efficient catalyst compared to monometallic **Ba-ACM-4** MOF and TBAPy linker. Irradiation at 440 nm is crucial for achieving optimal results, as higher wavelengths (480 and 540 nm) led to significantly lower yields (Table S28, Supporting Information). The proposed mechanism involves the one-electron oxidation of Co(II) complex A to form a high-valent Co(III) intermediate B, facilitated by **ACM-4** and O_2 under visible light irradiation (Scheme S4, Supporting Information). Intermediate B, in the presence of a base, undergoes *ortho*-C–H activation to form intermediate C, followed by olefin coordination (D)

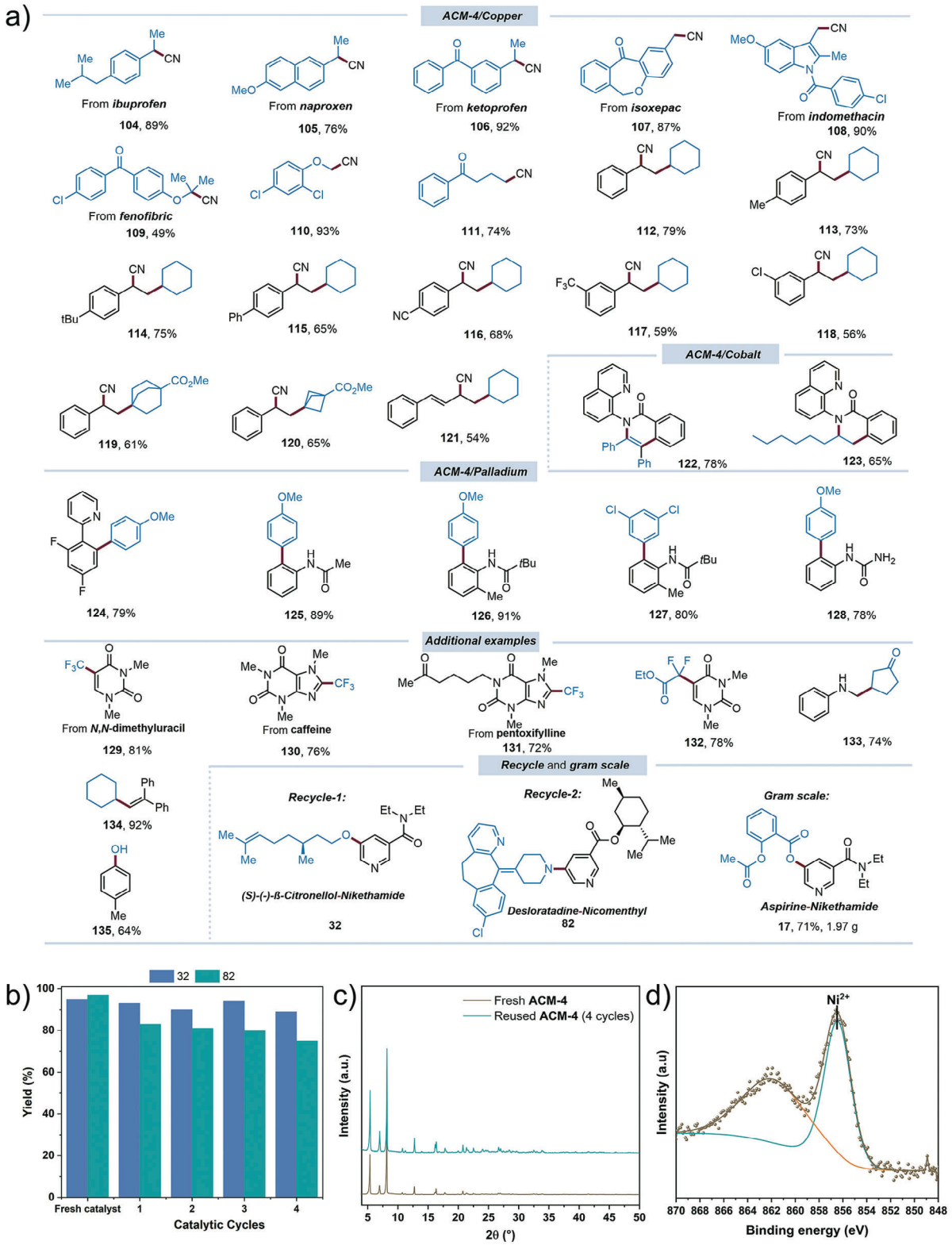

Figure 6. a) Substrate scope and evolution of strategies for various (dual) **ACM-4** photoredox/transition metal-catalyzed cross-coupling and SET reactions. b) Catalyst recycling. c) PXRD patterns of **ACM-4** before and after four catalytic cycles. d) XPS spectrum of **ACM-4** after four catalytic cycles. The symbols are the experimental data, while the full lines are the components used for the decomposition of the spectra. See the Supporting Information for detailed reaction conditions for each substrate; yields are isolated.

and subsequent annulation (E), leading to the desired annulated product.

2.4. ACM-4/Pd Photoredox Dual Catalysis

Following the successful integration of 3d transition metals with **ACM-4**, we also employed the 4d transition metal palladium in conjugation with **ACM-4** to efficiently catalyze the ortho-C–H activation in arenes. This method is effective with various directing groups, including pyridine, amide, and urea, yielding C–H arylation products **124–128** in good to excellent yields (Figure 6a). Control experiments confirm that both the **ACM-4** and Pd catalysts are crucial for product formation (Table S29, Supporting Information). A mechanism involving the formation of a palladacycle (aryl–Pd(II)) through C−H activation is speculated, where the aryl–Pd(II) captures the aryl radical ($PhN_2^+/Ph^\bullet$; $E_{1/2} = -0.10$ V vs SCE) generated by the **ACM-4**, forming a Pd(III) intermediate. This Pd(III) intermediate then undergoes SET oxidation, facilitated by the oxidized **ACM-4**, resulting in the regeneration of **ACM-4** and the formation of Pd(IV) active intermediate. The Pd(IV) species subsequently undergoes rapid reductive elimination, releasing the C−C cross-coupled product and regenerating the Pd(II) catalyst (Scheme S5, Supporting Information).

2.5. ACM-4 SET Catalysis with Organic Substrates

To further demonstrate the versatility of **ACM-4** as a photoredox catalyst, we explored its application in transition metal-free photoinduced radical addition reactions including trifluoromethylation, decarboxylative alkylation, and hydroxylation, which is expected to proceed via oxidative and reductive quenching pathways (Figure 6a). For instance, our method effectively enables late-stage fluoroalkylation of biologically active molecules, providing a range of fluoroalkylated products **129–132** with excellent yields. Similarly, **ACM-4** proves to be a highly effective heterogeneous photoredox catalyst under diverse decarboxylative conditions, facilitating alkyl radical addition reactions with remarkable yields (**133-134**). Notably, **ACM-4** demonstrates excellent reactivity in the presence of molecular oxygen under standard reaction conditions, enabling the oxidative hydroxylation of 4-methylboronic acid to produce 4-methylphenol (**135**) with a moderate yield of 64%. This hydroxylation reaction is initiated through the reduction of O_2 ($E_{1/2} = O_2/O_2^{\bullet-} = -0.57$ V vs SCE) by **ACM-4**, resulting in the formation of boronic acid-superoxide radical anion and **ACM-4**$^{\bullet+}$. Concurrently, the oxidation of $^iPr_2NEt$ by **ACM-4**$^{\bullet+}$ generates $^iPr_2NEt^{\bullet+}$ ($E_{1/2} = {}^iPr_2NEt/{}^iPr_2NEt^{\bullet+} = +0.72$ V vs SCE) and regenerates **ACM-4**, a process supported by preliminary quenching studies (Scheme S6, Figure S34, Supporting Information).

Overall, **ACM-4**′s ability to activate multiple transition metals (Ni, Cu, Co, and Pd) and the organic substrates under photochemical conditions is a distinctive and significant feature. Most photosensitizers have limited compatibility with certain organic substrates and transition metals due to mismatches in redox potentials or inefficient triplet energies. For instance, in our current study, the H_4TBAPy linker (a molecular analog of the **ACM-4** MOF) absorbs visible light and is compatible with Ni but not with Cu, Co, or Pd. This suggests that while it can reduce Ni(II), it is unable to oxidize Cu(I), Co(II), or Pd(III). In contrast, **ACM-4** effectively sensitizes a range of transition metals (Ni, Cu, Co, and Pd), and a variety of organic substrates enabling diverse catalytic processes without destabilizing radical intermediates. Additionally, **ACM-4**′s versatility-characterized by its stability, selectivity, and large bandgap-contribute to its capacity to function in both energy and electron transfer mechanisms.

2.6. Gram-Scale Synthesis and Recyclability

To demonstrate the scalability of the present methodology using **ACM-4**, a gram-scale (2 g, 7.78 mmol) reaction was conducted using aspirin and 5-bromo nikethamide with low loading of **ACM-4** (30 mg), which gave the aspirin-nikethamide C−O cross-coupled product **17** in 71% yield (Figure 6a). One notable advantage of using MOFs in catalysis is their reusability and ease of separation from the reaction mixture, which sets them apart from other solid photocatalysts. After the reaction, **ACM-4** was recovered through centrifugation, purified by simple washing, and reused in subsequent cycles (see supporting information for details). Although some nickel deposition on the **ACM-4** could potentially affect its photocatalytic activity and optical properties, **ACM-4** demonstrated excellent recyclability without a significant loss of photocatalytic activity (for the synthesis of **32** and **82**) over up to four cycles (Figure 6b). However, for compound **82**, a slight decrease in photocatalytic activity was observed in each catalytic cycle, likely due to the deposition of a small amount of amine impurities on the **ACM-4** catalyst during the reaction. Additionally, the recovered **ACM-4** (after the fourth cycle) was characterized by PXRD and XPS. The PXRD pattern of the reused **ACM** showed that the integrity of the MOF structure was retained (Figure 6c). XPS analysis revealed no formation of Ni nanoparticles during the reaction, as evidenced by the absence of the Ni^0 band at 852.0 eV (Figure 6d). Instead, the XPS spectrum of the reused **ACM-4** showed a single band in the Ni 2p region at 856.4 eV (Ni $2p_{3/2}$),[27] corresponding to Ni(II) species. It is worth mentioning that the content of nickel, as determined by ICP-OES, was 1.3 wt.%, corresponding to Ni that was not removed during the recovery process. In addition, XPS analysis confirmed the presence of Ti^{4+} (458.8 eV) and Ba^{2+} (780.1 eV) species (Figure S17, Supporting Information), indicating that **ACM-4** maintains its structural integrity and high stability throughout the process. This structural stability strongly suggests that **ACM-4** can function as a single-platform photo(redox)catalyst, capable of activating multiple transition metal catalysts and supporting a wide array of catalytic processes. It can incorporate a diverse range of substrates, including more challenging coordinating molecules. This versatility is particularly valuable for synthetic applications, especially from an industrial perspective, as it demonstrates **ACM-4**′s ability to accommodate a range of functional groups and molecular frameworks.

3. Conclusion

Unlike homogeneous iridium or ruthenium-based photocatalysts, which face significant challenges related to scalability and

recyclability, we have developed a new heterogeneous catalyst, **ACM-4**, based on a Ba/Ti MOF. This catalyst stands out as an exceptionally versatile photosensitizer for a wide range of late-stage functionalization reactions. **ACM-4** offers a promising alternative to conventional photosensitizers and is distinguished by its environmentally friendly, scalable, and cost-effective nature. Its broad redox potential range, from +1.11 to −1.49 V versus saturated calomel electrode (SCE), enables the reduction or oxidation of various organic substrates and transition metals such as Ni, Cu, Co, and Pd. Additionally, the triplet energy of **ACM-4** is comparable to or higher than the commonly used conventional photosensitizers, which warrants its use as an energy transfer photocatalyst. Notably, **ACM-4** can be easily recovered and reused multiple times with minimal loss in efficiency. The efficacy of this Ba/Ti MOF is demonstrated through its ability to drive a variety of organic transformations, including carbon-heteroatom cross-coupling reactions involving pharmaceuticals, agrochemicals, and natural products. These significant findings underscore the potential of **ACM-4** as a highly versatile and cost-effective photoredox catalyst, offering a one-material sustainable solution for efficient chemical processes. These newly developed methodologies can enhance environmental sustainability and increase the economic feasibility of catalytic drug development reactions, facilitating industrial implementation and significantly contributing to photocatalysis, metal catalysis, and sustainable chemistry.

Supporting Information

Supporting Information is available from the Wiley Online Library or from the author.

Acknowledgements

K.M., I.S.K., and L.G-T. contributed equally to this work. K.N.L. and C.H.H. acknowledge support from the National Science Foundation under grant no. 2237345 and the Camille and Henry Dreyfus Foundation.

Conflict of Interest

The authors declare no conflict of interest.

Data Availability Statement

The data that support the findings of this study are available in the supplementary material of this article.

Keywords

cross-coupling, metal organic framework, photocatalysis

Received: April 20, 2024
Revised: November 18, 2024
Published online:

[1] a) S. P. Pitre, L. E. Overman, *Chem. Rev.* **2022**, *122*, 1717; b) A. Y. Chan, I. B. Perry, N. B. Bissonnette, B. F. Buksh, G. A. Edwards, L. I. Frye, O. L. Garry, M. N. Lavagnino, B. X. Li, Y. Liang, E. Mao, A. Millet, J. V. Oakley, N. L. Reed, H. A. Sakai, C. P. Seath, D. W. C. MacMillan, *Chem. Rev.* **2022**, *122*, 1485; c) D. C. Fabry, M. Rueping, *Acc. Chem. Res.* **2016**, *49*, 1969; d) M. Parasram, V. Gevorgyan, *Chem. Soc. Rev.* **2017**, *46*, 6227.

[2] A. Savateev, I. Ghosh, B. König, M. Antonietti, *Angew. Chem., Int. Ed.* **2018**, *57*, 15936.

[3] a) I. Ghosh, J. Khamrai, A. Savateev, N. Shlapakov, M. Antonietti, B. König, *Science* **2019**, *365*, 360; b) Y. Cai, Y. Tang, L. Fan, Q. Lefebvre, H. Hou, M. Rueping, *ACS Catal.* **2018**, *8*, 9471; c) S. Reischauer, V. Strauss, B. Pieber, *ACS Catal.* **2020**, *10*, 13269; d) S. Mazzanti, A. Savateev, *Chem. Plus. Chem.* **2020**, *85*, 2499; e) S. Gisbertz, S. Reischauer, B. Pieber, *Nat. Catal.* **2020**, *3*, 611; f) Y. Lin, J. Guo, J. San Martin, C. Han, R. Martinez, Y. Yan, *Chem. Eur. J.* **2020**, *26*, 13118; g) B. Pieber, J. A. Malik, C. Cavedon, S. Gisbertz, A. Savateev, D. Cruz, T. Heil, G. Zhang, P. H. Seeberger, *Angew. Chem., Int. Ed.* **2019**, *58*, 9575; h) D. C. Fabry, J. Zoller, M. Rueping, *Org. Chem. Front.* **2019**, *6*, 2635; i) C. Cavedon, A. Madani, P. H. Seeberger, B. Pieber, *Org. Lett.* **2019**, *21*, 5331; j) A. Vijeta, C. Casadevall, S. Roy, E. Reisner, *Angew. Chem., Int. Ed.* **2021**, *60*, 8494; k) K. Muralirajan, R. Kancherla, J. A. Bau, M. R. Taksande, M. Qureshi, K. Takanabe, M. Rueping, *ACS Catal.* **2021**, *11*, 14772; l) L. Xing, Q. Yang, C. Zhu, Y. Bai, Y. Tang, M. Rueping, Y. Cai, *Nat. Commun.* **2023**, *14*, 1501.

[4] a) Y.-Y. Zhu, G. Lan, Y. Fan, S. S. Veroneau, Y. Song, D. Micheroni, W. Lin, *Angew. Chem., Int. Ed.* **2018**, *57*, 14090; b) A. Jati, K. Dey, M. Nurhuda, M. A. Addicoat, R. Banerjee, B. Maji, *J. Am. Chem. Soc.* **2022**, *144*, 7822; c) A. López-Magano, B. Ortín-Rubio, I. Imaz, D. Maspoch, J. Alemán, R. Mas-Ballesté, *ACS Catal.* **2021**, *11*, 12344; d) G. Lan, Y. Quan, M. Wang, G. T. Nash, E. You, Y. Song, S. S. Veroneau, X. Jiang, W. Lin, *J. Am. Chem. Soc.* **2019**, *141*, 15767; e) X. Yu, S. M. Cohen, *J. Am. Chem. Soc.* **2016**, *138*, 12320; f) Y. Quan, W. Shi, Y. Song, X. Jiang, C. Wang, W. Lin, *J. Am. Chem. Soc.* **2021**, *143*, 3075.

[5] a) A. Dhakshinamoorthy, Z. Li, H. Garcia, *Chem. Soc. Rev.* **2018**, *47*, 8134; b) L. Zeng, X. Guo, C. He, C. Duan, *ACS Catal.* **2016**, *6*, 7935.

[6] J. G. Santaclara, F. Kapteijn, J. Gascon, M. A. van der Veen, *CrystEngComm* **2017**, *19*, 4118.

[7] H. L. Nguyen, *New J. Chem.* **2017**, *41*, 14030.

[8] F. P. Kinik, A. Ortega-Guerrero, D. Ongari, C. P. Ireland, B. Smit, *Chem. Soc. Rev.* **2021**, *50*, 3143.

[9] A. Cadiau, N. Kolobov, S. Srinivasan, M. G. Goesten, H. Haspel, A. V. Bavykina, M. R. Tchalala, P. Maity, A. Goryachev, A. S. Poryvaev, M. Eddaoudi, M. V. Fedin, O. F. Mohammed, J. Gascon, *Angew. Chem., Int. Ed.* **2020**, *59*, 13468.

[10] a) C. A. Bravo-Sanabria, L. C. Solano-Delgado, L. M. Valdivieso-Zarate, R. Ospina-Ospina, F. Martínez-Ortega, G. E. Ramírez-Caballero, *Mol. Catal.* **2023**, *545*, 113240; b) C. D. Wagner, NIST X-Ray Photoelectron Spectroscopy Database, *NIST Standard Reference Database Number 20*, National Institute of Standards and Technology, Gaithersburg, MD, USA **2000**, p. 20899.

[11] K. Fabrizio, K. A. Lazarou, L. I. Payne, L. P. Twight, S. Golledge, C. H. Hendon, C. K. Brozek, *J. Am. Chem. Soc.* **2021**, *143*, 12609.

[12] N. Kolobov, A. Zaki, K. Świrk, P. Maity, L. Garzon-Tovar, G. K. Angeli, A. Dikhtiarenko, G. Delahay, P. N. Trikalitis, A.-H. Emwas, A. Cadiau, O. F. Mohammed, C. H. Hendon, K. Adil, J. Gascon, *ACS Mater. Lett.* **2023**, *5*, 1481.

[13] G. Capano, F. Ambrosio, S. Kampouri, K. C. Stylianou, A. Pasquarello, B. Smit, *J. Phys. Chem. C* **2020**, *124*, 4065.

[14] F. P. Kinik, A. Ortega-Guerrero, F. M. Ebrahim, C. P. Ireland, O. Kadioglu, A. Mace, M. Asgari, B. Smit, *ACS Appl. Mater. Interfaces* **2021**, *13*, 57118.

[15] a) N. A. Romero, D. A. Nicewicz, *Chem. Rev.* **2016**, *116*, 10075; b) C. K. Prier, D. A. Rankic, D. W. C. MacMillan, *Chem. Rev.* **2013**, *113*, 5322.

[16] a) C. Zhu, H. Yue, J. Jia, M. Rueping, *Angew. Chem., Int. Ed.* **2021**, *60*, 17810; b) E. B. Corcoran, M. T. Pirnot, S. Lin, S. D. Dreher, D.

A. DiRocco, I. W. Davies, S. L. Buchwald, D. W. C. MacMillan, *Science* **2016**, *353*, 279; c) E. R. Welin, C. Le, D. M. Arias-Rotondo, J. K. McCusker, D. W. C. MacMillan, *Science* **2017**, *355*, 380; d) T. Kim, S. J. McCarver, C. Lee, D. W. C. MacMillan, *Angew. Chem., Int. Ed.* **2018**, *57*, 3488.

[17] H. Luo, Y. Feng, L. Lin, *ChemCatChem* **2023**, *15*, 202300303.

[18] a) P. S. Baran, *J. Am. Chem. Soc.* **2018**, *140*, 4751; b) D. G. Brown, J. Boström, *J. Med. Chem.* **2016**, *59*, 4443.

[19] a) S. Tabassum, A. F. Zahoor, S. Ahmad, R. Noreen, S. G. Khan, H. Ahmad, *Mol. Divers* **2022**, *26*, 647; b) L. Guillemard, N. Kaplaneris, L. Ackermann, M. J. Johansson, *Nat. Rev. Chem.* **2021**, *5*, 522.

[20] a) E. A. Meyer, R. K. Castellano, F. Diederich, *Angew. Chem., Int. Ed.* **2003**, *42*, 1210; b) T. J. Ritchie, S. J. F. Macdonald, R. J. Young, S. D. Pickett, *Drug. Discov. Today* **2011**, *16*, 164.

[21] A. Barker, J. G. Kettle, T. Nowak, J. E. Pease, *Drug. Discov. Today* **2013**, *18*, 298.

[22] T. Wang, L. Zhang, J. Liu, X.-X. Li, L. Yuan, S.-L. Li, Y.-Q. Lan, *Chem. Commun.* **2022**, *58*, 7507.

[23] a) B. Ma, J. Zhang, K. Lin, D. Li, Y. Liu, X. Yang, *ACS Sustain. Chem. Eng.* **2019**, *7*, 13569; b) L. Luo, D. Li, Y. Dang, W. Wang, G. Yu, J. Li, B. Ma, *ACS Sustain. Chem. Eng.* **2022**, *10*, 5949; c) N. Kolobov, L. Garzon-Tovar, T. Shoinkhorova, G. Shterk, S.-H. Chung, A. Rendón-Patiño, A. Alfaraidi, J. Ruiz-Martínez, C. H. Hendon, J. Gascon, *J. Catal.* **2024**, *431*, 115370.

[24] a) C. A. Kent, D. Liu, L. Ma, J. M. Papanikolas, T. J. Meyer, W. Lin, *J. Am. Chem. Soc.* **2011**, *133*, 12940; b) N. A. Till, L. Tian, Z. Dong, G. D. Scholes, D. W. C. MacMillan, *J. Am. Chem. Soc.* **2020**, *142*, 15830.

[25] R. Kancherla, K. Muralirajan, B. Maity, S. Karuthedath, G. S. Kumar, F. Laquai, L. Cavallo, M. Rueping, *Nat. Commun.* **2022**, *13*, 2737.

[26] J. A. Malik, A. Madani, B. Pieber, P. H. Seeberger, *J. Am. Chem. Soc.* **2020**, *142*, 11042.

[27] L. Chen, Y. Jiang, H. Huo, J. Liu, Y. Li, C. Li, N. Zhang, J. Wang, *Appl. Catal. A: Gen.* **2020**, *594*, 117457.